High Resolution Imaging and Spectroscopy Using C_S-corrected TEM with Cold FEG JEM-ARM200F

C. Ricolleau[†], J. Nelayah[†], T. Oikawa[†, ††], Y. Kohno[††], N. Braidy[†, †††], G. Wang[†], F. Hue[†] and D. Alloyeau[†]

[†] **Laboratoire Matériaux et Phénomènes Quantiques, Université Paris Diderot/CNRS**
[††] **JEOL Ltd.**
[†††] **Laboratoire d'Etude des Microstructures, ONERA-CNRS**

Recently, at the University Paris Diderot (France), a unique in the world electron microscope configuration was installed. It consists of a JEOL JEM-ARM200F spherical aberration corrected electron microscope (TEM) equipped with a cold field emission gun (CFEG). In this paper, we report on the performances of this newly developed 80 - 200 kV microscope. Firstly, we show that the stability of both emission and probe currents makes the use of this new cold-FEG much friendlier. Energy spread of electrons emitted from the CFEG has been measured as a function of emission current and shows a very last 0.26 eV energy resolution at 200 kV and even 0.23 eV at 80 kV. The combination of the cold FEG and the CEOS aberration corrector of the objective lens, associated to enhanced mechanical and electrical stabilities of this new TEM, allows reaching a point resolution of 75 pm at 200 kV and 80 pm at 80 kV. This unseen point resolution at 200 kV has allowed us to study the structure of CoPt nanoparticles by observing direct images of their atomic arrangement along high indexes zone axis, as well as carbon graphite along the [0001] zone axis orientation. The high sensitivity of this microscope allows us to image and to analyze the chemical specie of single atoms diffusing on an amorphous carbon substrate. Finally, we used the small energy spread of the CFEG to study the surface plasmon resonance modes characteristic of bimetallic nanoparticles in close electromagnetic interaction.

Introduction

The understanding of physical and chemical properties of nanomaterials requires to investigate their structural and chemical arrangements at the atomic scale. For that purpose, Transmission Electron Microscope (TEM) is the most complete characterization instrument because it gives access to all these structural aspects on individual nano-objects [1-3]. In the past, conventional high resolution TEM has given numerous information on the structural properties of nanomaterials, however, the resolution was limited to 0.18 nm at 200 kV for the best optical configuration (namely magnetic lens with a low gap pole piece). Thanks to the revolutionary development of aberration corrected TEM, the attainable spatial resolution can now be of the picometer order [4-8]. This ability to resolve distances of less than 0.1 nm is very important in order to characterize new metallic, semi-conductor, oxides, … nanostructures for which 0.1 nm is of the same order of magnitude than the distances between atoms in many zone axis orientation of interest in these materials. Huge progresses in quantitative TEM have also been done due to the recent development of highly coherent electron sources [9-11]. Among the electron sources with a narrow energy spread around a tenth of an eV [12-14], the high brightness of Cold Field Emission Gun (CFEG) is a tremendous advantage for the study of nanomaterials, in which poor elastic and inelastic signals emitted by small volumes of matter are key limiting factors. So far, highly coherent electron waves emitted from CFEG technology was applied to electron holography observation [15] and to the analysis of EELS fine structures [16].

The present work describes the performances of an unseen 80 - 200 kV microscope, employing a CFEG and an aberration-corrected objective lens. The capabilities of this instrument were used to determine the structure of bimetallic nanoparticles (NPs) from high index zone axis orientation, to visualize fragile carbon graphite structure, to image and to identify individual metal atoms on a surface of amorphous carbon and to measure the plasmon resonance modes in two interacting bimetallic CuAu nanoparticles.

Performances of the cold field emission gun (CFEG)

The CFEG developed in this work, employs a tungsten single crystal emitter with a <310> oriented axis. In order to keep high vacuum level in vicinity of the emitter, three non-evaporative getter (NEG) pumps are installed in the gun chamber [17]. Total evacuation speed of the NEGs corresponds to 300 (= 3×100) L/s. The accelerating tube is evacuated by 200 L/s sputter ion pump (SIP). Additionally, two intermediate chambers are designed using small orifices, in order to create a differential pumping system between gun chamber and column. These

UMR 7162, Case 7021, 75205 Paris Cedex 13, France

E-mail: Christian.Ricolleau@univ-paris-diderot.fr

intermediate chambers are also evacuated by 20 L/s and 30 L/s SIPs, respectively [17]. The newly designed evacuation system can provide a vacuum better than 5×10^{-9} Pa, at the bottom of the accelerating tube. Owing to high quality of the vacuum, high stabilities of both emission and probe currents are expected. **Figure 1** shows variations of emission and probe currents after flashing procedure of the tip. Decay rate of probe current was less than 5% in the first 2 hours after flashing. Since the probe current takes only into account electrons emitted by the (310) facets on the tungsten tip, the probe current is more stable than total emission current [18].

Figure 2a shows zero-loss peak measurements at various emission current conditions, obtained with a Quantum ER Gatan Imaging Filter®. The energy spread of the electron source is commonly defined by the full width at half maximum (FWHM) of the zero-loss peak, measured without specimen. The energy spread depends on the emission current due to the statistical Coulomb effect [19-20]. The energy spread varies from 0.26 eV with an emission current of 0.1 μA to 0.4 eV in normal emission current conditions (20 μA). As illustrated in Figure 2b, the energy resolution measurements are even better with an accelerating voltage of 80 kV, since the energy spread ranges from 0.35 eV in normal emission current conditions to 0.23 eV with an emission current of 0.1 μA. The smallest energy spread obtained here is close to the theoretical value at the emitter surface (0.22 eV). This result shows that the high-voltage stability (5×10^{-7} min^{-1} peak-to-peak fluctuation) is high enough to maintain the energy spread of the CFEG.

Microscope performances

The objective lens of the TEM used in this experiment has inherent optical performances as listed in **Table 1**. In this newly developed TEM, a CEOS hexapole type spherical aberration corrector [4] was employed. Therefore, the final spherical aberration coefficient (C_S) can be tuned from –0.1 mm to +0.5 mm with a precision of about 1 μm. The lens excitation current of objective lens has a stability of 5×10^{-7} min^{-1} in peak-to-peak fluctuation. To evaluate the aberrations of the image-forming system, a diffractogram tableau [21] with a maximum tilt angle of 24 mrad was employed. **Table 2** shows a list of residual aberrations calculated in the procedure.

Figure 3a demonstrates the achieved point resolution of the microscope in these imaging conditions. A high resolution image of a carbon film was doubly exposed with small shift of field of view induced by projector alignment deflector. The

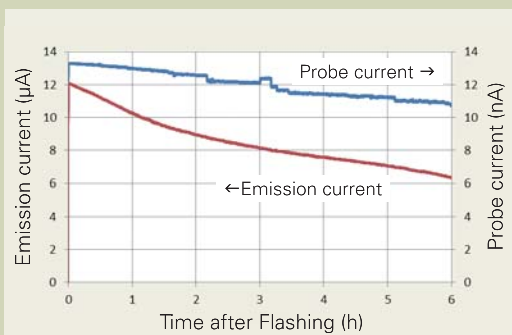

Fig. 1 Variations of emission (μA) and probe (nA) currents after flashing procedure. Decay rate of probe current was less than 5% in the first 2 hours after the flashing.

Table 1 Inherent optical performances of objective lens employed in the TEM.

Item	Performance
Focal length (f_0)	1.9 mm
Spherical aberration coefficient (C_s)	0.5 mm
Chromatic aberration coefficient (C_c)	1.1 mm
Minimum focus step (Δf)	0.25 nm
Lens current fluctuation (peak-to-peak) (ΔI)	5×10^{-7} min^{-1}

Table 2 Residual aberrations calculated by the CEOS aberration corrector software.

Residual aberration	Value
Defocus (C_1)	- 184.7 nm
Two-fold astigmatism (A_1)	140.6 pm
Three-fold astigmatism (A_2)	23.0 nm
Axial coma (B_2)	7.1 nm
Spherical aberration coefficient (C_3)	- 518.3 nm
Four-fold astigmatism (A_3)	146.1 nm
Star aberration (S_3)	167.1 nm
Five-fold astigmatism (A_4)	40.1 μm

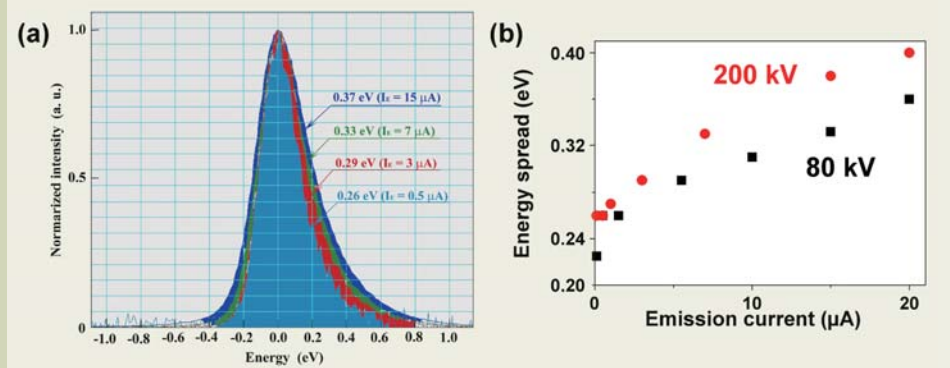

Fig. 2 (a) Measured zero-loss peaks at various emission current (I_E) conditions. The energy spread was defined by FWHM of the zero-loss peak. (b) Energy spread as a function of emission current measured at 200 kV (red circles) and at 80 kV (black squares).

Fourier transform of this image gives the well known Young's fringes pattern which shows a point resolution of 75 pm. This resolution was measured with the commonly used minimum contrast level of 13.5%. Such a performance is close to the theoretical limit for a 200 kV TEM. Figure 3b shows the Fourier transform of a lattice image of a gold single crystal in [100] zone axis orientation. This image highlights that the microscope attains a lattice resolution of 46 pm, since the (048) reflection of the gold lattice is clearly observed. Figure 3c shows the Young's fringes pattern obtained with similar optical parameters at 80 kV. In spite of this low voltage condition, the point resolution of the microscope reaches 80 pm. The possibility to maintain sub-angstrom imaging resolution with an energy resolution below 0.4 eV at 80 kV opens many possibilities for the atomic scale characterization of beam sensitive materials.

Application data

Structural analysis of CoPt nanoparticles with the sub-angstrom resolution

Figure 4 shows calculated envelope functions of the contrast transfer function (CTF) for the cold and Schottky FEG by using the following parameters, namely $C_C = 1.1$ mm and $\Delta I/I = \Delta V/V = 5\times10^{-7}$. For the calculation, the energy spreads of 0.4 eV and 0.75 eV for cold and Schottky FEG were used, respectively, the accelerating voltage was 200 kV, the beam convergence angle was 2 mrad and the C_S value was close to zero. According to the calculated results, although the point resolution is limited to 0.1 nm for Schottky FEG it is expected to obtain a point resolution of 0.075 nm for CFEG. The resolution of 75 pm obtained in the experiment (Figure 3a) is in good agreement with the calculated one. Hence, by combining the C_S corrector, the CFEG and by using newly designed microscope column and power supplies, the C_S value, the beam coherency and the microscope stability have been optimized to reach sub-angstrom resolution and improve signal to noise ratio in the high spatial frequency range. Indeed, by minimizing the damping of the envelope functions, the reduction of both electron energy dispersion and mechanical vibration allow a sub-angstrom information transfer limit (Figure 4). Thus high resolution imaging is not limited anymore for the structural study of low index crystal orientations: today one can resolve many more inter-planar distances and thus displays the structure of materials in many more orientations. This highly improved resolution is very important to study the size effect on the structural properties of individual nano-objects. This major advantage is illustrated in **Figure 5**a in which the structure of a CoPt nanoparticles in the [114] zone axis orientation is directly observed on the C_S corrected high resolution image and an information transfer up to the –440 reflection (65 pm) is reported on the Fourier transform (Figure 5b).

Graphite

In the previous section, we have seen that the performances of the JEOL JEM-ARM200F cold FEG are almost the same at 80 kV than the ones at 200 kV. It is thus possible to observe nanomaterials which are sensitive to electron beam such as polymers and carbon

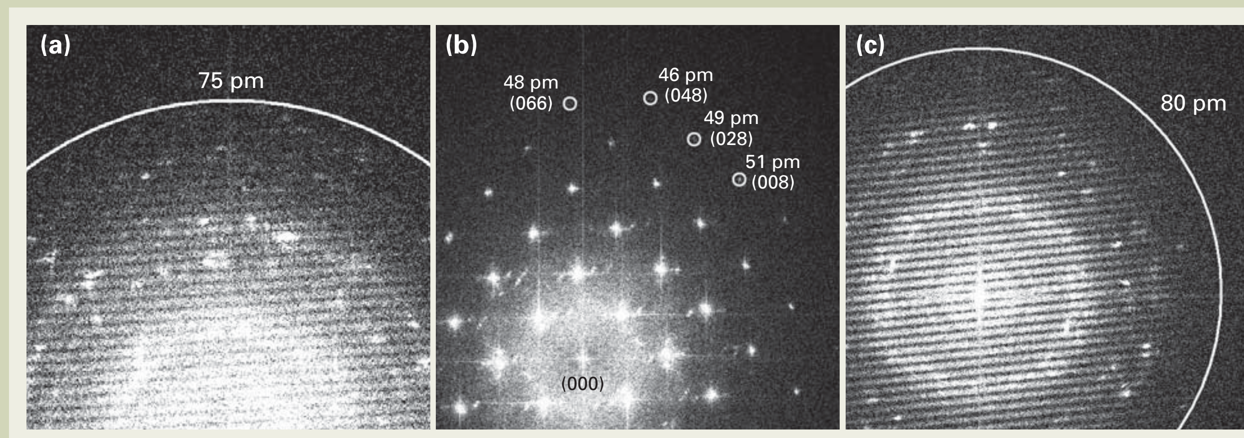

Fig. 3 (a) Young fringes pattern obtained at 200 kV showing a point resolution of 75 pm. (b) Fast Fourier transformation (FFT) of a high resolution image obtained at 200 kV on a (100) gold single crystal. The observation of the [048] peak of the gold crystal highlights that the lattice resolution of the microscope is below 50 pm (d_{048} = 0.046 nm). (c) Young fringes pattern obtained at 80 kV showing a point resolution of 80 pm.

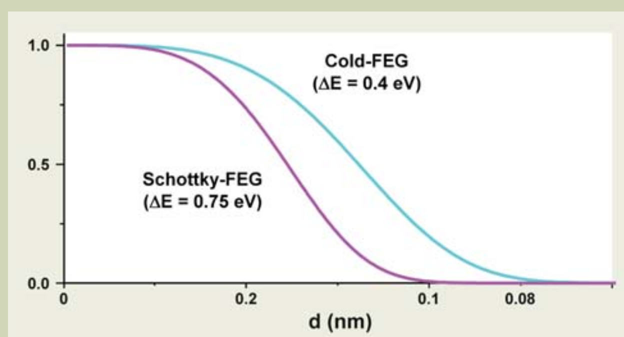

Fig. 4 Calculated envelope functions of the contrast transfer function (CTF) for cold (cyan) and Schottky (magenta) FEG by using the following parameters, namely $C_C = 1.1$ mm and $\Delta I/I = \Delta V/V = 5\times10^{-7}$. For the calculation, the energy spreads of 0.4 eV and 0.75 eV for the cold and Schottky FEG were used, respectively, the accelerating voltage was 200 kV, the beam convergence angle was 2 mrad and the C_S value was close to zero.

nanostructures. This instrument opens up the route to direct observations of the grafting of molecules on the surface on the nanotubes as well as to the determination of the electronic states of these hybrid nanostructures in order to study their structural and electronic properties.

As an example of fragile materials imaging, **Figure 6** shows high resolution images of carbon graphite oriented along the [0001] zone axis obtained at 80 kV, with a C_S value of 230 nm. Figure 6a shows a wide field of view of the sample where more or less dark contrasts are visible in the image. Those contrasts correspond to different layer steps of the graphite. The specimen is composed by the stacking of only a few layers of graphite. Figure 6b shows a diffractogram of the image (a), the spatial frequency (lattice resolution) of 71 pm was recorded. Figure 6c shows a magnified area from a part of the image in (a) marked by the white rectangle. Noise reduction was applied to the image by using a spatial annular filter in the power spectrum of the original image. Figure 6d shows the atomic model of the mono-layered graphite. By comparison with the experimental image, we clearly observed that the white contrast corresponds to carbon atom sites.

Single atom imaging

When the growth and coarsening of nanostructures composed of two or more chemical elements are concerned, the imaging and chemical identification of single atoms is of primary importance to understand coalescence and Ostwald ripening phenomena at the atomic scale. Furthermore, in the case of alloyed nanostructures, nanoparticle compositional changes may arise during growth or thermal annealing if the two species have different thermodynamic behavior. As an example, we have shown in a previous paper on CoPt bimetallic nanoparticles [22], that after a heat treatment at high temperature, the larger NPs present a large excess of Co. To understand the origin of this result, we have studied *in situ* the NPs coarsening by using the energy transferred from the electron beam to the nanoparticles. Typical HRTEM image of the CoPt NPs after a few seconds under beam irradiation is presented in **Figure 7**a. On this image, individual atoms appear as additional contrast in the carbon film between the NPs. However, these contrasts appear and disappear from frame to frame when image series are recorded with a 0.2 s time interval indicating that the diffusion of metallic atoms on carbon substrate is too fast to follow the path of a single atom from a particle to another. But, it is still possible to observe such diffusing atoms on HRTEM images because they are trapped long enough in energetically favorable site of the carbon thin film. In order to interpret this result and to determine the chemical nature of the atoms, comparison between experimental and simulated HRTEM images was performed. For that purpose, the atomic model consists in one Co and one Pt atom on a 5 nm-thick amorphous carbon film. To quantify the simulated and experimental contrast of single atoms in the images, we used the signal to noise ratio (SNR) definition proposed by Rose [23]. The SNR is defined as the ratio between the incremental change in the image intensity due to the atoms and the standard deviation of the carbon film intensity (defined as the noise level). We calculated the SNR as a function of the objective lens defocus for both Co and Pt atoms and we have shown that the SNR is flat against the defocus in a range from –2 to –10 nm and that the contrast difference between Co and Pt is significant: from –2 to –2.6 for Co and from –3 to –3.6 for Pt. These simulations allow us to determine the optimum optical condition for the chemical analysis of single atoms. The analysis of the single atom contrast was firstly performed on pure Co and Pt NPs to calibrate the experimental conditions. The histograms of the SNR of single atoms for both samples are shown on **Figure 8**. These histograms are centered on –2.68 for Co atoms and –3.18 for Pt atoms, with a standard deviation of 0.18 and 0.30 respectively. These values are in good agreement with simulations. On CoPt nanoparticles, as shown in Figure 7a, both Co and Pt atoms were detected during the beam induced NPs coarsening. The first profile (green intensity profile in Figure 7b) reveals the presence of a Co atom on the carbon film (SNR of –2.32) whereas the second profile (blue intensity profile on Figure 7c) shows a Pt atom (SNR of –3.59). These results show that, using these illumination conditions, the energy transferred from the electron beam to the CoPt NPs allows overcoming the energy barrier for atomic evaporation from a NP to the substrate either for Co or Pt atoms. Furthermore, a statistical analysis realized by measuring the SNR of 100 single atoms clearly shows that the kinetic of atomic exchange is faster for Co than Pt. Indeed, among the 100 analyzed atoms, 61 are Co, 32 are

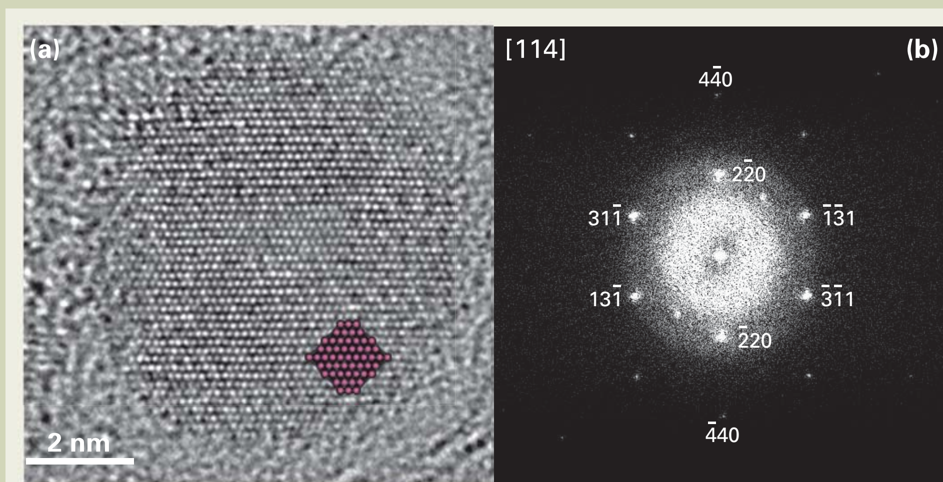

Fig. 5 (a) HRTEM image of a CoPt nanoparticle observed along the [114] zone-axis orientation (C_S=0.005 mm, Δf=–0.5 nm (Scherzer focus), focus spread of 2.2 nm). An inset (red) indicates an atomic model on the projectd plane. (b) Corresponding power spectrum of the HRTEM image (a).

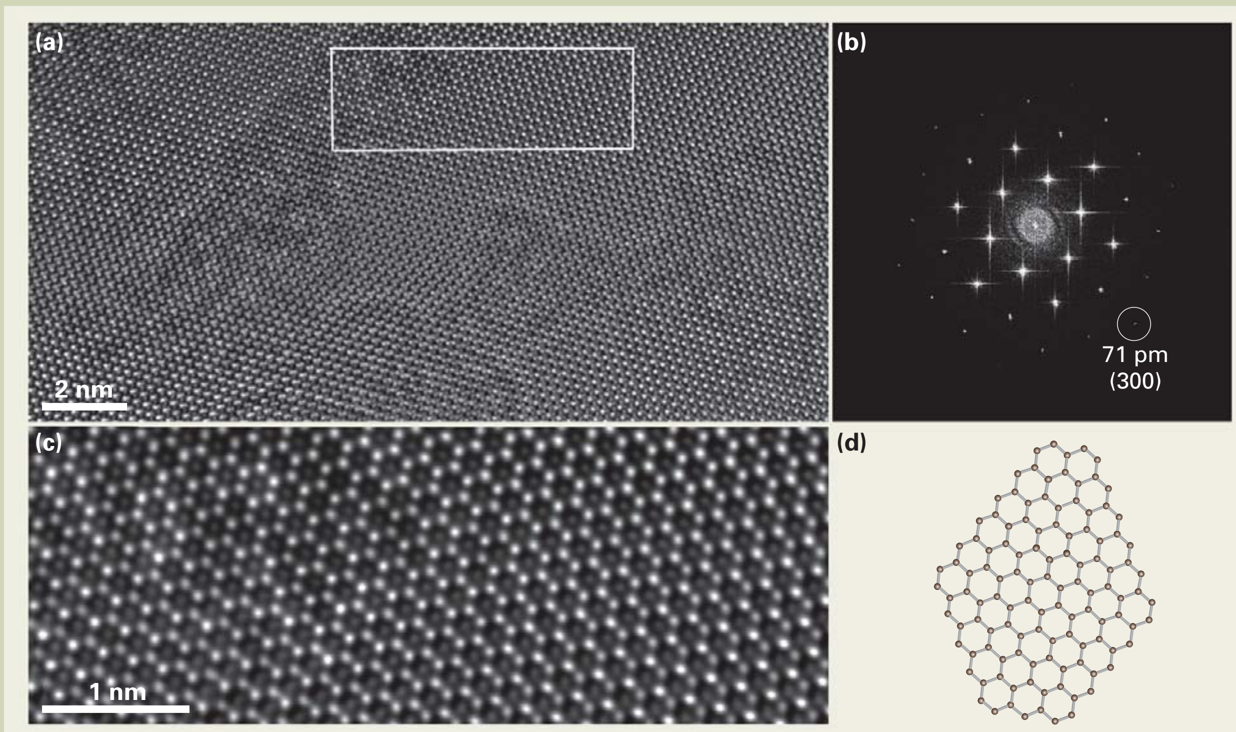

Fig. 6 (a) HRTEM image of a carbon graphite crystal oriented along the [0001] zone axis obtained at 80 kV. (b) Fourier transform of the image (a). (c) Magnified area corresponding to the white rectangle in image (a). The image was obtained by applying a spatial filter to the original image (a). (d) Atomic model of a mono-layered graphite crystal.

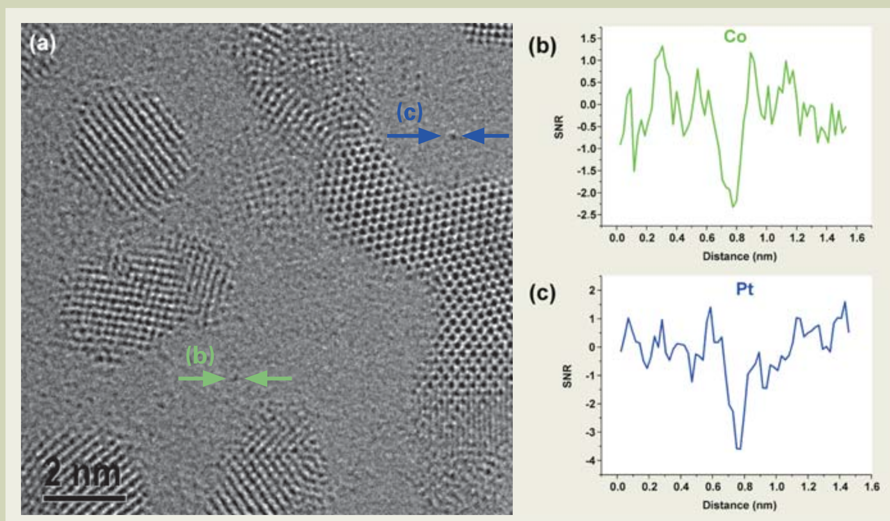

Fig. 7 (a) HRTEM image of CoPt nanoparticles. Individual Co and Pt atoms appear as additional black contrast on the carbon substrate. Signal to noise ratio (SNR) measured between the two corresponding arrows in (a) for both Co and Pt atoms: (b) SNR profile showing one Co atom (SNR of –2.32). (c) SNR profile showing one Pt atom (SNR of –3.59).

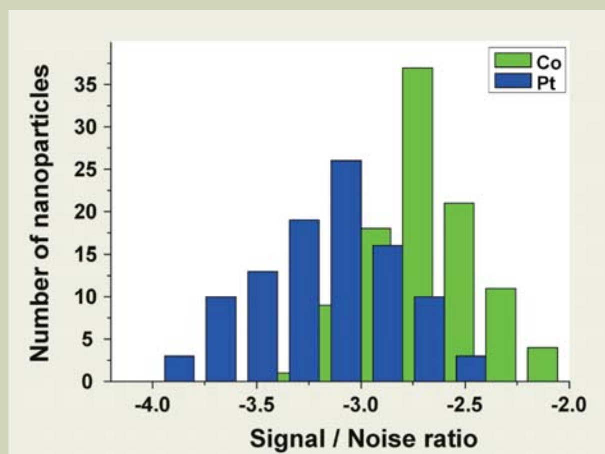

Fig. 8 Histogram of the single atom SNR experimentally measured for pure Co NPs (green) and pure Pt NPs (blue).

Pt and 7 are undetermined. These results explain the size dependant composition changes in CoPt NPs and highlight the better mobility of Co atoms with respect to Pt atoms because of their higher evaporation rate. These results show that the sensitivity of the microscope enhanced by the high brightness of the cold FEG and the mechanical stability of the ARM200F, allows distinguishing the chemical nature of individual Co and Pt atoms while they are diffusing on the surface of the carbon substrate. In this study, the modulation transfer function (MTF) of the Gatan CCD camera was not taken into account because we always use the same magnification in order to have the same MTF effects in all the HRTEM images. It is however possible to improve the quantitative agreement between experimental and simulated single atom contrast by accounting this MTF on the experimental images [24].

Plasmon resonance nanospectroscopy in metallic nanoparticles

Metallic nanoparticles have shown to exhibit unique optical properties. The latter result from the existence of collective electronic excitations, known as surface plasmon resonances (SPRs), under electromagnetic excitations (for instance, light or fast electrons) [25]. Associated with these surface-bound resonances are intense electromagnetic fields which are exploited in various potential applications like surface-enhanced Raman scattering and all-optical communication. In the context of an electron microscope, nanometer-scale studies of SPRs in the visible spectral domain, where most of the potential applications lie, is now possible using electron energy loss spectroscopy [26-27]. Taking full advantage of the intense and highly monochromatic sources of electrons that is generated by the cold FEG JEOL JEM-ARM200F, our group has been using spatially-resolved STEM-EELS to investigate the optical response of either isolated or interacting metallic nanoparticles. **Figure 9**a shows an HAADF image of two carbon-supported gold-copper nanocubes in very close interaction (gap distance <1 nm). EEL spectra were acquired at different positions on the dimer with the following experimental conditions: the microscope was operated at 200 kV and with an initial energy resolution of about 0.4 eV (2.5 mm spectrometer entrance aperture, camera length 3 cm and 0.05 eV/pix dispersion). To increase the signal-to-background ratio in the visible domain, the raw data was subsequently deconvoluted using a non-linear iterative algorithm [28]. The spatial resolution, fixed by the probe size, was better than 1 nm (spot size 5C). Figure 9b compares STEM-EEL spectra acquired at five distinct positions on the dimer. The position, at which each numbered spectrum is acquired, is indicated by red dots in Figure 9a. Two distinct modes centered at about 2.30 eV and 2.60 eV are detected at the outer corners and in the gap region respectively. Comparison of the EELS data shows these SPRs are common to the two nanocubes (the dimer) though they are not identical. This results from the electromagnetic coupling between the nanocubes when they are brought in interaction. Such analysis illustrates the power of STEM-EELS to finely study the optical properties of nanoparticles with the aim of tailoring these properties for targeted applications.

Conclusion

The JEOL JEM-ARM200F cold FEG TEM described in this paper is the first commercial instrument combining both a cold field emission electron source and a CEOS aberration corrector of the objective lens. We have shown the very good stability of both emission and probe currents thanks to a new design of the vacuum system for the gun chamber including non evaporating getter pumps. The combination of the JEOL cold FEG and the CEOS aberration corrector, associated to enhanced mechanical and electrical stabilities of the instrument allows reaching a point resolution of 75 pm at 200 kV and 80 pm at 80 kV. Owing to high coherency of electron waves and high stabilities of both electrical and mechanical part on the TEM developed in this work, much smaller lattice spacing information that the point resolution were excited in the interferences of the waves. In addition, the high brightness of the cold FEG substantially improved imaging sensitivity that is essential for quantitative high resolution imaging.

We have shown that sub-angstrom imaging is of great benefit for understanding the structural properties of nanomaterials, because it is now possible to observe crystals and defects along high index zone axis orientation. We have also demonstrated that the performances of the microscope can be exploited for studying the mobility of single atoms on surface which is very useful for the understanding of crystal growth and crystal reshaping, as well as the understanding of the coalescence and Ostwald ripening phenomena at the atomic scale. Finally, we

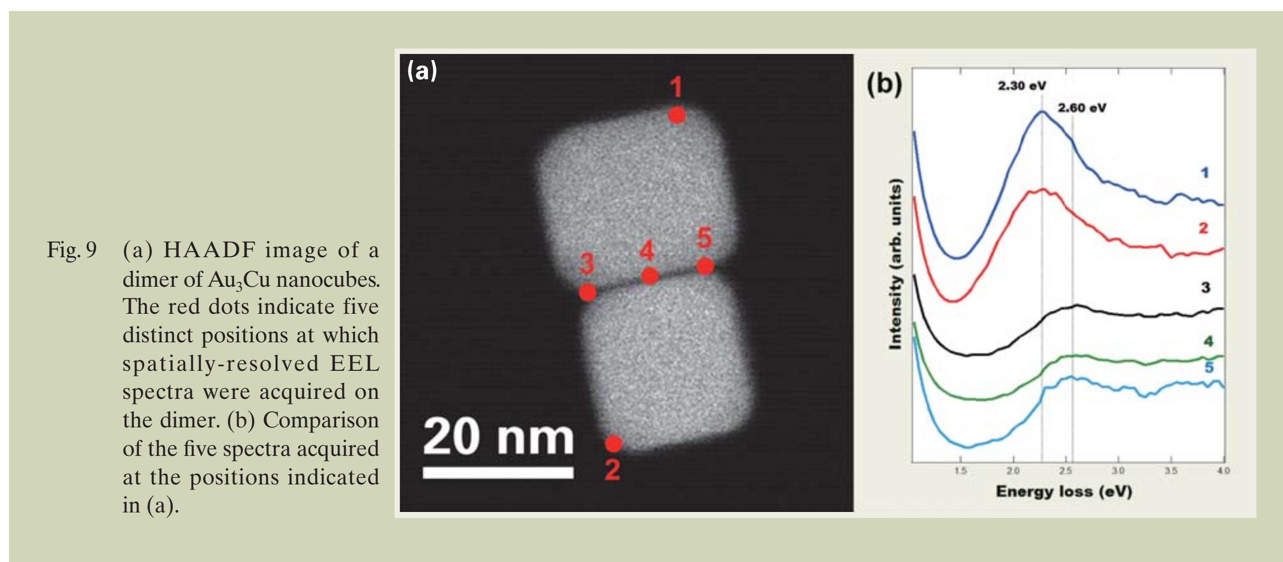

Fig. 9 (a) HAADF image of a dimer of Au_3Cu nanocubes. The red dots indicate five distinct positions at which spatially-resolved EEL spectra were acquired on the dimer. (b) Comparison of the five spectra acquired at the positions indicated in (a).

showed how the small energy spread of the cold FEG can be successfully used to measure surface plasmon resonance modes characteristic of metallic nanoparticles which are close enough to exhibit electromagnetic interactions.

Acknowledgments

Financial support from ANR within ANR-07-NANO-018-04 (ETNAA) is gratefully acknowledged. The authors are indebted to Dr Dario Taverna (IMPMC, University Paris 6, Paris, France) for providing us the graphene / graphite sample.

References

[1] Kirkland A.I. Nanocharacterisation. Royal Society of Chemistry, Cambridge. (2007).

[2] Reimer L. Transmission Electron Microscopy. Springer, Berlin. (1997).

[3] Shindo D. and Hiraga K. High-Resolution Electron Microscopy for Materials Science. Springer Verlag, Tokyo. (1998).

[4] Haider M., Uhlemann S., Schwan E., Rose H., Kabius B. and Urban K. Electron microscopy image enhanced. *Nature* **392**: 768-769 (1998).

[5] Krivanek O.L., Dellby N. and Lupini A.R. Towards sub-Angstrom electron beams. *Ultramicroscopy* **78**: 1-11 (1999).

[6] Urban K. Studying Atomic Structures by Aberration Corrected Transmission Electron Microscopy. *Science* **321**: 506-510 (2008).

[7] Kisielowski C., Freitag B., Bischoff M., Van Lin H., Lazar S., Knippels G., Tiemeijer P., Van Der Stam M., Von Harrach S., Stekelenburg M., Haider M., Uhlemann S., Müller H., Hartel P., Kabius B., Miller D., Petrov I., Olson E.A., Donchev T., Kenik E.A., Lupini A.R., Bentley J., Pennycook S.J,. Anderson I.M., Minor A.M., Schmid A.K., Duden T., Radmilovic V., Ramasse Q.M., Watanabe M., Erni R., Stach E.A., Denes P. and Dahmen U. Detection of Single Atoms and Buried Defects in Three Dimensions by Aberration-Corrected Electron Microscope with 0.5-Å Information Limit. *Microscopy and Microanalysis* **14**: 469-477 (2008).

[8] Takayanagi K., Kim S., Lee S., Oshima Y., Tanaka T., Tanishiro Y., Sawada H., Hosokawa F., Tomita T., Kaneyama T. and Kondo Y. Electron microscopy at a sub-50 pm resolution. In: *Journal of Electron Microscopy,* pp. S239-S244) (2011).

[9] Browning N.D., Arslan I., Erni R., Idrobo J.C., Ziegler A., Bradley J., Dai Z., Stach E.A. and Bleloch A. Monochromators and aberration correctors: Taking EELS to new levels of energy and spatial resolution. In: *EMAG-NANO 2005: Imaging, Analysis and Fabrication on the Nanoscale*, eds. Brown P D, Baker R and Hamilton B, pp. 59-64, (Iop Publishing Ltd, Bristol) (2006).

[10] Kimoto K., Ishizuka K., Asaka T., Nagai T. and Matsui Y. 0.23 eV energy resolution obtained using a cold field-emission gun and a streak imaging technique. *Micron* **36**: 465-469 (2005).

[11] Kimoto K., Kothleitner G., Grogger W., Matsui Y. and Hofer F. Advantages of a monochromator for bandgap measurements using electron energy-loss spectroscopy. *Micron* **36**: 185-189 (2005).

[12] Browning N.D., Arslan I., Erni R., Idrobo J.C., Ziegler A., Bradley J., Dai Z., Stach E.A. and Bleloch A. Monochromators and aberration correctors: Taking EELS to new levels of energy and spatial resolution. In: *EMAG-NANO 2005: Imaging, Analysis and Fabrication on the Nanoscale,* eds. Brown P D, Baker R and Hamilton B, pp. 59-64, (Iop Publishing Ltd, Bristol) (2006).

[13] Kimoto K., Ishizuka K., Asaka T., Nagai T. and Matsui Y. 0.23 eV energy resolution obtained using a cold field-emission gun and a streak imaging technique. *Micron* **36**: 465-469 (2005).

[14] Kimoto K., Kothleitner G., Grogger W., Matsui Y. and Hofer F. Advantages of a monochromator for bandgap measurements using electron energy-loss spectroscopy. *Micron* **36**: 185-189 (2005).

[15] Tonomura A. Applications of electron holography. *Rev. Mod. Phys*. **59**: 639-669 (1987).

[16] Chen S.Y., Gloter A., Zobelli A., Wang L., Chen C.H. and Colliex C. Electron energy loss spectroscopy and ab initio investigation of iron oxide nanomaterials grown by a hydrothermal process. *Phys. Rev. B* **79**: 104103 (2009).

[17] Kohno Y., Okunishi E., Tomita T., Ishikawa I., Kaneyama T., Ohkura Y., Kondo Y. and Isabell. T. Development of a Cold field-Emission Gun for a 200 kV Atomic Resolution Electron Microscope. *Microscopy and Analysis Nanotechnology* **24**: S9-S13 (2010).

[18] Kasuya K., Katagiri S., Ohshima T. and Kokubo S. Stabilization of a tungsten <310> cold field emitter. *Journal of Vacuum Science & Technology B: Microelectronics and Nanometer Structures* **28**: L55-L60 (2010).

[19] Jansen G.H. *Coulomb interaction in particle beams.* Academic Press Inc. (1990).

[20] Tiemeijer P.C. Measurement of Coulomb interactions in an electron beam monochromator. *Ultramicroscopy* **78**: 53-62 (1999).

[21] Zemlin F., Weiss K., Schiske P., Kunath W. and Herrmann K.H. Coma-free alignment of high resolution electron microscopes with the aid of optical diffractograms. *Ultramicroscopy* **3**: 49-60 (1978).

[22] Alloyeau D., Prévot G., Le Bouar Y., Oikawa T., Langlois C., Loiseau A. and Ricolleau C. Ostwald ripening in nanoalloys : when thermodynamics drives a size-dependent particle composition. *Phys. Rev. Letters*, **105**, 255901 (2010).

[23] Rose A., Advances electronics and electron physics. Academic Press, New York, (1948).

[24] A. Thust, High-Resolution Transmission Electron Microscopy on an Absolute Contrast Scale. *Physical Review Letters* **102**, 220801 (2009).

[25] Kreibig U. and Vollmer M. Optical Properties of Metal Clusters, volume 25 of Springer Series in Material Science. Springer, Germany, (1995).

[26] Bosman M., Keast V. J., Watanabe M., Maaroof A. I. and Cortie M.B. Mapping Surface Plasmons at the Nanometre Scale with an Electron Beam. *Nanotechnology* **18**, 165505 (2007).

[27] Nelayah J., Kociak M., Stephan O., J.Garcia de Abajo F., Tence M., Henrard L., Taverna D., Pastoriza-Santos I., Liz-Marzan L.M., and Colliex C. Mapping surface plasmons on a single metallic nanoparticle. *Nature Physics* **3** (5) :348–353 (2007).

[28] Gloter A., Douiri A., Tencé M. and Colliex C. Improving energy resolution of EELS spectra: an alternative to the monochromator solution. *Ultramicroscopy* **96**: 385–400 (2003).